Identification of Local Extinction and Prediction of Reignition in a Spark-Ignited Sparse Spray Flame using Data Mining

Andrew P. Wandel

The University of Southern Queensland,
School of Mechanical and Electrical Engineering,
Toowoomba, 4350, Australia

Fax: +61 7 4631 2526; E-mail: andrew.wandel@usq.edu.au

Abstract

Direct Numerical Simulations (DNS) of droplet fields which are ignited using a spark are investigated to deduce any behaviour that distinguishes between the cases where successful flame propagation occurs and where a flame ignites but subsequently extinguishes. At the instant the spark was deactivated, some of the studied cases displayed no local extinction, others showed some local extinction (one with reignition and the rest with global extinction) and the rest showed global extinction. The gaseous field at this instant was analysed using the data mining technique the Gaussian Mixture Model on each case separately; this method groups data points, enabling distinction between the various behaviours. The results from this analysis showed that in the case with local extinction-reignition, the regions of space near the flame kernel which produced local quenching were caused by evaporating droplets. These regions of local quenching were relatively small compared to the strong flame front surrounding them; the regions of local quenching were also relatively far from the centre of the flame kernel. In contrast, in cases with local then global extinction, the droplets created regions which were extensions of the relatively-small flame front, and these regions behaved in a similar manner to the flame propagation. As a consequence, these cases were unable to support a self-sustaining flame. Such distinctive behaviour promises opportunities to detect situations where global extinction is imminent and implement appropriate control strategies to prevent global extinction.

Keywords: Direct Numerical Simulations, DNS, Spark Ignition, Sprays,

1. Introduction

The behaviour of spray flames under the influence of spark ignition is important for direct-injection engines [1] and gas turbine relight. Direct-injections engines are particularly receiving a lot of recent attention because of their potential to reduce emissions compared to port injection. An experimental study into the effects of equivalence ratio on a lean hydrous-ethanol engine [2] varied the leanness of the mixture and advanced the injection timing to compensate for the increased ignition delay as leanness increased. They observed a critical equivalence ratio which provided the maximum fuel efficiency and reduction in pollutants. Mixtures closer to stoichiometric had similar combustion phase durations, while leaner mixtures had increasing combustion phase durations. In another study [3], Rayleigh scattering was used to determine that injecting the fuel in two separate parcels improved the mixing compared to a single parcel with the same total mass, with consequential improvements in combustion. Two-parcel injections were also investigated [4] using PIV (Particle Image Velocimetry) to measure the effects on the turbulence caused by varying the injection timings. Adjusting the first injection timing produced a local minima in mean peak pressure for an intermediate timing, which also displayed the most cycle-to-cycle variability in IMEP and worst early flame development. This was likely due to the second injection interfering with the flow pattern created by the first. Advancing the second injection timing reversed the direction of the tumble flow, simultaneously strengthening it.

Two experimental investigations which are targeted at improving simulations of engines are now reviewed. One studied the fluid flow adjacent to the walls, which requires algebraic approximations in simulations in order for the computational time to obtain the solution to be tractable; some improvements were devised [5]. The other focussed on the nature of the turbulent eddies for four different fuels, providing invaluable information to enable simulations to match the conditions inside an engine [6].

Some recent investigations into the fundamental behaviour of sprays will be reviewed next. An experimental investigation studied the breakup of moderately-dense spray injections, characterising the behaviour of the various sizes of liquid structures formed in the evaporation process and subsequent combustion [7]. Another experimental study compared the behaviour

of palm biodiesel with Jet-A1 (standard jet fuel) to support the possibility of a biofuel for the aerospace industry [8]. A modelling study investigated the nature of an n-dodecane spray flame, reporting detailed information about the structure of the flow, behaviour of the combustion and mechanisms for flame success [9]. A Large Eddy Simulations (LES) investigation studied a series of ethanol flames, validating the results against experiments before providing information about the nature of the combustion [10]. Experimental [11] and LES [12] studies found that the location of the spark needs to be carefully chosen so that conditions are suitable for successful ignition.

Due to the complexities in the gaseous scalar field induced by the discrete nature of the droplet field and the evaporation rate [13], the large variations in gradients pose challenges for modelling [14, 15]. Detailed Numerical Simulations also show that large gradients prevent ignition of single droplets in high-temperature regions [16].

While Direct Numerical Simulation (DNS) provides a powerful tool for investigating such phenomena [15], it is limited by currently-available computational resources (both memory and processing power). Two approaches are utilised: one resolves the turbulent gaseous scales (the Kolmogorov length scale for the gas, as done in single-phase DNS) and either the droplets are modelled as point sources of mass whose diameters are significantly smaller than the grid resolution, e.g. Refs. [17, 18, 19, 20, 21, 22, 23, 24, 25], or larger droplets and droplet structures are simulated using models such as the Volume of Fluid (VOF) method and level-set method, e.g. Refs. [26, 27, 28]. The other approach fully-resolves the liquid phase with the limitation of only simulating a few tiny droplets [29, 30, 31, 32, 33].

The current work uses the first approach to investigate the causes for spark-ignited spray cases extinguishing. Few papers investigate spark ignition, and those that do focus primarily on ignition behaviour, not extinction. The author has previously investigated extinction in spark-ignition cases with a qualitative measure [34] and a quantitative measure [35] to determine flame success being found. The approach taken in the current work is to use a data mining technique to analyse the gaseous fields at the instant the spark is deactivated to discriminate between regions of space that promote flame propagation and those which produce quenching. Note that droplet evaporation naturally produces local quenching, with the potential for providing a state that will support flame propagation. It has previously been suggested [35] that for cases which promote a self-sustaining flame, there is a distinction between a "burning" branch (regions which promote a self-sustaining flame

front) and an "extinguishing" branch (regions which cause local extinction). For flames which ignited, but subsequently extinguished, there was no such distinction near the core of the flame kernel. The objective in this paper is to categorically determine whether the regions of local quenching are distinct from the regions of self-sustaining flame propagation and investigate the causes of this separate behaviour. If these regions are distinct, then this enables identification of regions of local extinction which will reignite in the future, as opposed to causing global extinction.

2. Theory

2.1. DNS code

A 3-D compressible DNS code called SENGA was used [36, 37, 38, 39, 40]. Complete details of the code and simulations investigated here can be found in Ref. [35]; a summary will be provided here. The gas-phase transport equations for continuity, momentum, total energy, fuel and oxidiser are:

$$\frac{\partial \rho}{\partial t} + \frac{\partial \rho U_i}{\partial x_i} = \dot{d}_F \tag{1}$$

$$\frac{\partial \rho U_j}{\partial t} + \frac{\partial \rho U_i U_j}{\partial x_i} = -\frac{\partial p}{\partial x_j} + \frac{\partial \sigma_{ji}}{\partial x_i} + \dot{d}_{v_j} \tag{2}$$

$$\frac{\partial \rho e}{\partial t} + \frac{\partial \rho U_i e}{\partial x_i} = -\frac{\partial p U_i}{\partial x_i} + \frac{\partial}{\partial x_i}\left(\frac{\mu C_P^g}{\mathrm{Pr}}\frac{\partial T}{\partial x_i}\right) + \frac{\partial \sigma_{ik} U_k}{\partial x_i} + W_E + \dot{q}''' + \dot{d}_e \tag{3}$$

$$\frac{\partial \rho Y_F}{\partial t} + \frac{\partial \rho U_i Y_F}{\partial x_i} = \frac{\partial}{\partial x_i}\left(\frac{\mu}{\mathrm{Sc}}\frac{\partial Y_F}{\partial x_i}\right) - W_F + \dot{d}_F \tag{4}$$

$$\frac{\partial \rho Y_O}{\partial t} + \frac{\partial \rho U_i Y_O}{\partial x_i} = \frac{\partial}{\partial x_i}\left(\frac{\mu}{\mathrm{Sc}}\frac{\partial Y_O}{\partial x_i}\right) - W_O\,. \tag{5}$$

Here p is pressure; σ_{ji} the stress tensor; μ the dynamic viscosity of the gaseous phase; C_P^g the specific heat at constant pressure of the gaseous phase; Pr the Prandtl number; W_φ the various chemical source terms; Y_F and Y_O the mass fractions of fuel and oxidiser respectively; and Sc the Schmidt number. The non-dimensionalised temperature is

$$T = \frac{\hat{T} - \hat{T}_0}{\hat{T}_{\mathrm{ad}} - \hat{T}_0} \tag{6}$$

with $\hat{T}_{\rm ad}$ the adiabatic flame temperature at the stoichiometric condition and $\hat{T}_0$ the initial temperature. The spark source term $\dot{q}'''$ is modelled by a Gaussian distribution based on the distance from the centre of the domain and is constant in time for the spark duration

$$t_{\rm sp} = bt_F \,. \tag{7}$$

The spark duration parameter was chosen to be $b = 0.2$, while the characteristic laminar flame timescale $t_F = l_F/S_L$ is calculated from the laminar flame speed S_L and the characteristic laminar flame thickness

$$l_F = D/S_L \tag{8}$$

where D is the unburned gas diffusivity.

A single-step irreversible chemical mechanism is used for W_φ [38]

$$\text{Fuel} + s\,\text{Oxidizer} \rightarrow (1+s)\,\text{Products}\,, \tag{9}$$

where s is the mass of oxidiser per unit of mass of fuel at stoichiometric conditions. The consumption rate of fuel is given by an Arrhenius-type expression:

$$W_F = B^* \rho Y_F Y_O \exp\left[-\frac{\beta(1-T)}{1-\alpha(1-T)}\right] \tag{10}$$

where β is the Zel'dovich number, given by

$$\beta = \frac{E_a(\hat{T}_{\rm ad} - \hat{T}_0)}{R_u \hat{T}_{\rm ad}^2}\,. \tag{11}$$

The activation energy is E_a, while R_u is the universal ideal gas constant. In Eq. (10), α is a heat release parameter given by

$$\alpha = \frac{\tau}{1+\tau} \tag{12}$$

$$\tau = \frac{\hat{T}_{\rm ad} - \hat{T}_0}{\hat{T}_0}\,, \tag{13}$$

while B^* is

$$B^* = B\exp(-\beta/\alpha)\,, \tag{14}$$

with B the pre-exponential factor.

The various droplet source terms (due to droplet evaporation and transport) are calculated by

$$\dot{d}_\varphi = -\frac{1}{V}\sum_d \frac{dm_d\varphi_d}{dt} \tag{15}$$

where V is the volume of the DNS cell and m_d the mass of each droplet which influences the DNS node of interest. The droplet transport uses the method of Réveillon and Vervisch [17]. The droplets are transported through space according to their velocity

$$\frac{d\mathbf{x}_d}{dt} = \mathbf{v}_d\,, \tag{16}$$

which relaxes to the interpolated value of gaseous velocity at the droplet location:

$$\frac{d\mathbf{v}_d}{dt} = \frac{\mathbf{U}(\mathbf{x}_d,t) - \mathbf{v}_d}{\tau_d^p}\,. \tag{17}$$

The droplet temperature similarly relaxes to the interpolated value of gaseous temperature and also has a sink term due to evaporation

$$\frac{dT_d}{dt} = \frac{T(\mathbf{x}_d,t) - T_d - B_d L_v/C_p^g}{\tau_d^T}\,. \tag{18}$$

Here B_d is the Spalding number, obtained based on the fuel mass fraction and the Clausius–Clapeyron equation using unity Lewis number (Le) and T_d [35]; while L_v is the latent heat of vaporisation. The loss of droplet mass due to evaporation is modelled by the decay of the droplet diameter a_d:

$$\frac{da_d^2}{dt} = -\frac{a_d^2}{\tau_d^v}\,. \tag{19}$$

All of the relaxation timescales τ_d^φ are proportional to a_d^2; τ_d^T and τ_d^v are functions of B_d; with other coefficients essentially constant after the initial evaporation [35].

2.2. DNS setup

The computational domain was a 128^3 cube of side length $L = 21l_F$. Partially non-reflecting (NSCBC) boundary conditions [41] were used for the x-direction, while the y- and z-dimensions were considered to be periodic. The first- and second-order spatial derivatives were computed using 10th-order central-difference schemes, which reduce to 2nd-order one-sided derivatives

at the non-reflecting boundaries. A third-order, low-storage Runge–Kutta scheme [42] was used for time advancement. A pseudo-spectral method [43] was used to generate the initial turbulent velocity field using the Batchelor–Townsend spectrum [44]. The velocity field was considered to be homogeneous and decaying.

The droplets of n-heptane were initially distributed uniformly in space throughout the y- and z-directions and in the central half of the x-direction. The remaining quarter of the volume between each side of the droplet region and the partially non-reflecting boundaries was taken to be pure air because the boundary conditions for droplets entering the computational domain through these boundaries are difficult to specify. The gaseous phase was initialised to be pure air throughout the domain and both phases were set to a constant temperature of $\hat{T}_0 = 500$ K.

The mixture fraction was defined as [45]

$$Z = \frac{Y_F - Y_O/s + Y_{O,i}/s}{Y_{F,i} + Y_{O,i}/s}\,, \tag{20}$$

where $Y_{F,i}$ is the fuel mass fraction in its inlet stream, $Y_{O,i}$ is the oxidiser mass fraction in its inlet stream and s is the stoichiometric mass ratio of oxidiser to fuel. The following are the values for the current case:

$$Y_{F,i} = 1.0 \tag{21}$$

$$Y_{O,i} = 0.233 \tag{22}$$

$$s = 3.52\,, \tag{23}$$

with a stoichiometric mixture fraction of:

$$Z_{\rm st} = 0.062\,. \tag{24}$$

The reaction progress variable is defined as

$$c = \frac{(1-Z)Y_{{\rm O},i} - Y_{\rm O}}{(1-Z)Y_{{\rm O},i} - \max\left(0, \frac{Z_{\rm st}-Z}{Z_{\rm st}}\right) Y_{{\rm O},i}} \tag{25}$$

where $c = 0$ represents no reactions and 1 represents complete chemical reactions. Its scalar dissipation is

$$N_{cc} = D\nabla c \cdot \nabla c\,. \tag{26}$$

The behaviour of N_{cc} with respect to c will be investigated in this paper.

2.3. Data mining method

The Gaussian Mixture Model (GMM) is a density-based method used to find clusters of arbitrary shape for data that is n-dimensional [46]. A cluster is defined to be a collection of data points which are considered to have similar properties (with a total of M clusters; M is a parameter that must be chosen). Each cluster contains data points that are close together in the space of the chosen variables, so the data points in each cluster can be considered to behave similarly, while data points from a different cluster can be considered to behave differently. Each data point has a probability of belonging to each cluster and is allocated to the cluster to which it is most likely to belong. The probability is calculated based on a Gaussian joint-probability density function (jpdf) in the n-dimensional space.

Because the data points are clustered based on Gaussian densities, in 2-D space elliptical shapes tend to be formed (within the boundaries of the possible values in space). When clusters overlap, one cluster is deemed to take priority over all the data points within the common region, so that cluster will penetrate into that region. It is also possible for data points to be completely separated from other data points in the same cluster if the penetrating cluster is sufficiently narrow.

The derivation of the GMM follows Ref. [47]. A GMM is a weighted sum of M component Gaussian densities:

$$P(\mathbf{x}|\lambda) = \sum_{i=1}^{M} w_i g(\mathbf{x}|\boldsymbol{\mu}_i, \boldsymbol{\Sigma}_i) \tag{27}$$

where M is the number of clusters; $\mathbf{x}$ is an n-dimensional, continuous-valued data vector; and w_i are the mixture weights, constrained by

$$\sum_{i=1}^{M} w_i = 1\,. \tag{28}$$

The component Gaussian densities (clusters) are n-dimensional Gaussian functions:

$$\begin{aligned} g(\mathbf{x}|\boldsymbol{\mu}_i, \boldsymbol{\Sigma}_i) &= \frac{1}{[(2\pi)^n |\boldsymbol{\Sigma}_i|]^{1/2}} \\ &\quad \times \exp\!\left(-\tfrac{1}{2}(\mathbf{x}-\boldsymbol{\mu}_i)'\boldsymbol{\Sigma}_i^{-1}(\mathbf{x}-\boldsymbol{\mu}_i)\right) \end{aligned} \tag{29}$$

where $\boldsymbol{\mu}_i$ is a vector containing the mean of the data points within cluster i (for each i, there are n values), with $\boldsymbol{\Sigma}_i$ the corresponding covariance matrix.

The parameters of the GMM are:

$$\lambda = \{w_i, \boldsymbol{\mu}_i, \boldsymbol{\Sigma}_i\} \quad i = 1, \ldots, M\,, \tag{30}$$

which are found iteratively using an Expectation-Maximisation (EM) algorithm. The first step (expectation) computes the *a posteriori* probability of data point j being in cluster i for each cluster:

$$\mathcal{P}(i|\mathbf{x}_j, \lambda) = \frac{w_i g(\mathbf{x}_j|\boldsymbol{\mu}_i, \boldsymbol{\Sigma}_i)}{P(\mathbf{x}_j|\lambda)}\,. \tag{31}$$

The maximisation step then estimates the parameters in λ using Maximum Likelihood Estimation (MLE) to maximise the likelihood of the GMM. In other words, for each data point, the probability of belonging to the chosen cluster is maximised. The new model for λ results in the maximal value of $P(\mathbf{x}|\lambda)$ being no smaller than the value from the previous model for λ, with iteration until the solution converges. During this process, data points can be allocated to different clusters depending on how the extents of the clusters are varied through the changes in λ.

The method used here to initialise λ was:

1. randomly choose M data points, indexed as k_i
2. set $\boldsymbol{\mu}_i = \mathbf{x}_{k_i}$
3. specify $\boldsymbol{\Sigma}_i$ to be diagonal, with the value for cluster i being the variance of $\mathbf{x}_{k_i}$; and
4. set $w_i = 1/M$.

Once λ has been determined, the cluster to which data point j is most likely to belong is determined by the value of i which returns the largest value of Eq. (31). This cluster identification forms the basis of the results presented here.

3. Results

The initial properties of the base case are described in Table 1, showing that the system is well resolved and contains a reasonable amount of turbulent energy. All the cases studied here are listed in Table 2 and are predominantly the same cases as studied in Ref. [35] (there are three additional

Table 1: Initial properties of base case: velocity fluctuations u', integral length scale L_{11}, spark duration $t_{\rm sp}$, characteristic chemical timescale $t_F = l_F/S_L$, average droplet evaporation time $t_{\rm evap}$, droplet number density ρ_n, Kolmogorov length scale η, droplet diameter a_d, grid cell size Δx and Taylor Reynolds number Re_λ.

u'/S_L	L_{11}/l_F	$t_{\rm sp}/t_F$	$t_{\rm evap}/t_F$	$(\rho_n)^{1/3}\eta$	η/l_F	a_d/l_F	$\Delta x/l_F$	Re_λ
4.26	4.50	0.200	1.95	0.475	0.315	0.0500	0.164	41.4

cases studied here—B1, B2 and KG—and the Base case is not labelled as B1). The Base case is so labelled because while it successfully burns throughout the current simulation, and would continue to do so for some time afterwards, it is marginally above the threshold for global extinction occurring. It therefore acts as a pivot for varying parameters to achieve different combustion regimes.

The purpose of adding cases B1 and B2 is to include some cases where combustion proceeds exceptionally well. A measure of the droplet number density is the Group Combustion Number

$$G = 3\left(1 + 0.276\mathrm{Re}_d^{1/2}\mathrm{Sc}^{1/3}\right)\mathrm{Le}\, n_c^{2/3}(a_d/s_d)\,. \tag{32}$$

Here n_c is the number of droplets in the cloud and s_d is the mean inter-droplet spacing. The parameters Re_d and n_c were chosen using the method of Ref. [48]: u' was used for the velocity in the former and the latter was the number of droplets within the sphere of radius R around the spark centre. Cases B1 and B2 have significantly higher droplet number density, and approach the regime of high G [49], while the remaining droplet cases have intermediate G. Cases B1, B2, BG and KG all show no evidence of local extinction; case Base shows local extinction-reignition behaviour; cases BE, I1, I2 and IG show local extinction followed by global extinction; while cases F1, F2 and FG only show global extinction behaviour (no ignition).

3.1. Mean plots

The turbulent kinetic energy (Fig. 1) has a modest decline up to the time of interest ($t_{\rm sp}$), with all cases performing similarly except for those with higher initial turbulence (cases KG and F2), which naturally have a higher rate of decay. The initial decay rate is not exponential due to the spark energy addition. The integral timescale for the base case is approximately $5t_{\rm sp}$, so the effects of turbulent transport do not dominate other effects, except in the higher-intensity cases KG and F2.

Table 2: Cases simulated. Names are: 'B' = 'Burned', 'I' = 'Ignited' and 'F' = 'Failed'; 1 and 2 are droplet cases, 'G' is for partially-premixed gaseous cases. Case Base successfully burned throughout the simulation and it is expected it would have continued burning for a substantial period beyond. Case BE is a droplet case that burned but would have extinguished after the simulation finished. Case KG is a gaseous case which successfully burned. The quantities reported at initial conditions are: local equivalence ratio in droplet initialisation region Φ, comparison of initial droplet diameter a_d to base case, and ratio of turbulent kinetic energy k to base case. The integral timescale t_L is reported at the instant the spark was deactivated and is normalised by the characteristic chemical timescale. G is the Group Combustion Number [49], Eq. (32).

Name	Φ	$(a_d/a_{d,b})^2$	k/k_b	t_L/t_F	G
B1	2.0	0.5	1	0.712	17.2
B2	4.0	1	1	0.706	19.8
BG	2.0	-	1	0.716	-
Base	2.0	1	1	0.724	7.8
BE	1.7	1	1	0.727	6.5
KG	2.0	-	8	0.483	-
I1	1.6	1	1	0.728	6.0
I2	2.0	1.5	1	0.732	5.1
IG	1.0	-	1	0.727	-
F1	1.0	1	1	0.735	3.6
F2	2.0	1	8	0.485	8.4
FG	0.5	-	1	0.735	-

The evaporation of the fuel can be demonstrated by the mean droplet diameter [Fig. 2, which is plotted to show the linear decay implied by Eq. (19)] and mixture fraction (Fig. 3). The effects of the spark and flame on the droplet diameter are reduced in Fig. 2 because droplets in those regions are vaporised almost instantaneously, so are removed from consideration. The smaller droplets in case B1 cause all the droplets to evaporate before the end of the simulation, allowing for enhanced burning capacity and complete combustion. In contrast, the increased droplet size in case I2 retarded the release of fuel, causing a failed flame. Comparing all the cases with the same droplet size (all droplet cases except for B1 and I2), the rate of evaporation for each droplet increased slightly as the droplet number density (ergo Φ and flame success) decreased (Fig. 2), but the overall mass evaporated decreased substantially (Fig. 3). The increased turbulence in case F2 had no effect on the droplet evaporation initially, but towards the end of the simulation it transported fuel out of the domain through the NSCBC boundaries. Under these conditions, the evaporation rate was able to slightly accelerate due to the lower fuel vapour pressure. The Favre-mean mixture fraction in the partially-premixed gaseous cases is not necessarily constant due to the change in density and the gas leaving the domain through the NSCBC boundaries.

The combined effects of the droplet evaporation and spark on the combustion are shown in the domain maximal temperature (Fig. 4) and Favre-mean temperature (Fig. 5). The only effects on the peak temperature achieved in the droplet cases were caused by decreased evaporation rate (cases B2 and I2) and lack of ignition (cases F1 and F2). Indeed, the maximal temperature in case B2 was suppressed throughout the simulation due to the increased evaporation load, which resulted in the mean temperature always being lower than the Base case's. However, despite the initial, substantial reduction in mean temperature caused by the accelerated evaporation in cases B1 and B2, both demonstrated an accelerated heat release rate by the end of the simulation. All the other droplet cases showed a decline in mean temperature.

3.2. Cluster plots

The results for the GMM are presented in this section. Many different variables—such as mixture fraction and its scalar dissipation (studied in Ref. [34]), and the cross-dissipation of mixture fraction and reaction progress variable—were analysed using GMM to determine any correlations. However, only the correlations observed in Ref. [35] between N_{cc} and c were found to provide significant differences between the types of cases. Other data mining

methods for clustering (the hierarchical method [46] and K-means clustering [50]) were unable to produce clusters that were distributed in a manner that enabled the current analysis.

The selection of M is the other major parameter to consider. If this number is too small, then there are insufficient clusters to distinguish between the burning and extinguishing branches; if M is too high, then the GMM will split all the cases into burning and extinguishing branches. Selecting a value of M that is too small would lead to errors by defining cases which clearly extinguish as cases which do not extinguish. On the other hand, selecting a value of M that is too large would classify cases which do not extinguish as cases which do extinguish. Since the primary purpose is to avoid global extinction, if M is too low, then the combustion could operate in an undesirable regime; however, if M is too large, then the combustion is guided into more strongly avoiding extinction. In a statistical representation of the problem, consider the hypothesis that a particular case burns successfully for the necessary duration. A value of M that is too low could cause a problematic Type I error (a "false positive") by being unable to distinguish between marginal cases and burning cases. However, a value of M that is too high could cause an acceptable but undesirable Type II error (a "false negative") by being unable to distinguish between marginal cases and extinguishing cases. The appropriate value for M is problem-dependent, so it is unlikely that the value used here will be suitable for all applications, but it is likely that a higher value will yield safer results.

The cluster plots for N_{cc} vs c (hence $n = 2$) in Fig. 6 show the data coloured by their respective cluster; the clusters are numbered so that the value of $\boldsymbol{\mu}_i$ for variable c monotonically increases with i. The value $M = 16$ was chosen here because it produced in case Base separation of the burning and extinguishing branches, without redundant clusters around $c = 1$. It is apparent that this choice of M produces redundant clusters near $c = 0$ for most cases and near $c = 1$ for the gaseous cases. The Supplemental Material contains the results for other choices of M: for $M \leq 10$ there is no separation of the burning and extinguishing branches in case Base (an unacceptable Type I error), while for $M > 34$ there is separation of the burning and extinguishing branches in case BE (an acceptable Type II error). If M is extremely large (e.g. $M = 50$), then the GMM creates multiple branches in all cases and the results again become unreliable, with every case potentially considered to have local extinction. Video 1 shows the convergence history of the GMM for $M = 16$. As the solutions evolve from the initial guess, there

are significant changes in $\boldsymbol{\mu}$ and $\boldsymbol{\Sigma}$, and it takes quite a few iterations for the final overall patterns to emerge.

The predominantly elliptical shape that was noted earlier can be seen in most of the clusters. The penetration of clusters into the region occupied by other clusters is denoted in Fig. 6 by the regions contained within the dashed ellipses. One example is cluster 6 in Fig. 6(d), which separates a few elements of cluster 9 from the vast majority and penetrates cluster 8. Other instances of nodes being separated from the rest of the cluster are cluster 7 in Fig. 6(a); 5, 7 and 8 in (b); and 11 in (h), which contains the maximum values of N_{cc} in addition to some of the lowest values of N_{cc} for some values of c.

Cases B1 and B2 [Fig. 6(a) and (b)] show distinctive behaviour compared to the rest of the droplet cases, with much narrower ranges of N_{cc} for a given value of c. They resemble the gaseous distributions in that there is normally a single cluster for a given value of c, except for the inevitable penetration of neighbouring clusters. The rest of the droplet cases (the left two columns) show layers of clusters for $0.2 < c < 0.8$, with the upper clusters tending to be above the results for case IG and the lower clusters tending to be below case IG. The upper clusters were previously identified as the "burning" branch, with the lower clusters the "extinguishing" branch [35]. The joint-probability density functions (jpdf) showed that the majority of elements were found in the lower clusters [35] and this bimodal behaviour is correctly captured by the GMM. The source of this bimodality will be investigated further in Sect. 3.3.

Figure 7 shows the primary point of interest, in terms of characterising the behaviour of the system. For $c > 0.8$, the burning and extinguishing branches are only distinct in the Base case [Fig. 6(d)], with the conditional mean from case IG providing a suitable delineator. This supports the previous conclusion that a distinctive separation of the branches is observed in cases where flame propagation has started to become successful, i.e. local extinction-reignition occurs [35]. This is a more generalised statement than the previous conclusions, since it is apparent that there is a finite transition from no ignition (always global extinction) to successful burning with no local extinction. Clearly there is some distinctive behaviour near the flame kernel, which enables some part of the flame front to be self-sustaining; this self-sustaining portion overcomes and ignites the portion which cannot sustain a flame.

The final interesting observation from the clusters in Fig. 6 is the behaviour of the gaseous simulations. Case BG [Fig. 6(c)] essentially has a

monotonic progression of cluster number with c, at lower N_{cc} than achieved by cases B1 and B2: the discrete nature of the droplet field creates higher gradients in the gaseous scalar field [13]. These higher gradients are necessary for successful flame propagation: if they are too low, then the flame thickness becomes too great and there is insufficient heat transfer through the flame to preheat the fluid ahead of the flame. Cases KG and IG [Fig. 6(f) and (i)] have broadly similar values of N_{cc} except for $c > 0.6$, where the successful KG case is significantly higher: this appears to be the critical region where higher gradients need to be present for successful flame propagation. This conclusion can be applied to the behaviour of the Base case, where the very few elements in cluster 8 does not affect the success of the flame. It is the very high proportion of elements in clusters 11 and 13 [the burning branch, indicated in Fig. 6(d)] {c.f. Figures 17(a) and 20(a) [35]} which produces success. It is the capacity of the droplet field to create locally-flammable regions despite overall equivalence ratios which would prevent combustion [51] which supports the Base case.

3.3. Physical visualisation

The flame structures observed in the presented cases will not occur identically in all similar cases, but they are predominantly caused by the rate of evaporation due to the droplet number density. Therefore, it is reasonable to assume that other, similar cases will form flame structures of similar complexity to those discussed in this section. To explain the behaviour observed in the previous section, the clusters are visualised in physical space in Fig. 8, which shows isosurfaces of $c = 0.96$ for all the cases, coloured by the clusters. (Video 2 shows the flame structure, starting from the centre of the flame kernel.) Droplets which are within one cell width of the isosurface are also displayed, and are directly responsible for most of the convex bumps on the surfaces. The majority of the surfaces of these bumps have locally-higher values of N_{cc} because the rapid evaporation of the droplets enables the flame kernels to stretch into regions with substantially lower values of c. It is apparent that the clusters are a patchwork, which is a consequence of physical space not being a variable in the GMM. However, there is a relatively-strong correlation between c and physical space (Figure 10 [35]) and the clusters are specified based on c, so the data points in each cluster are relatively close in physical space and are normally connected. For intermediate values of c, and particularly for cases BE and I1 [Fig. 8(e) and (g) respectively], there are obvious connections between locations based on the cluster number.

Figure 8(d) shows that the Base case is mostly represented by cluster 13; from Fig. 7(d), clusters 12 and 14 have very small values of N_{cc}, with the former extending down to $c \approx 0.87$ and the latter extending up to $c \approx 1$. Cluster 12 comes from the extinguishing branch and is predominantly observed in the promontories which are caused by evaporating droplets. In the base case, these regions are aberrations in the spherical shape imposed by the spark. Therefore, the evaporation is supported by the hot kernel and supplies fuel for a sufficiently-large volume (with consequential chemical reactions) that the spatial distribution of c is relatively stable. The heat sink of the evaporation causes these volumes to be part of the extinguishing branch, but spatially they were quite remote from the centre of the flame kernel, so did not instigate global extinction. Instead, reignition was able to occur.

In contrast, Fig. 8(e) and (g) show that cases BE and I1 are likely to have regions of high N_{cc} dominating the promontories (cluster 13 has exclusively-higher values of N_{cc} than cluster 14). There is a deficit of burned mixture surrounding these volumes (along any radial direction from the centre of the spark the value of c decreases with increasing radius, c.f. Figs. 9 and 10), hence their stretched nature. In addition to this difficulty, there is clear separation with a secondary structure which is the point of a much larger structure that partially wraps around the flame kernel at slightly lower values of c [see Figs. 9(e) and 10(e) as well as Video 2]. This is an under-developed kernel with no droplets in the near vicinity, so can only be a sink to the main kernel.

The multiple kernels which appear in case I2 [Fig. 8(h)] are part of a more complicated flame structure. It was previously observed that the primary structure is a sphere in the centre, with a horseshoe-shaped secondary structure and on the right of the image there is a small sphere in front of the horseshoe which is the tertiary structure [35]. At $c = 0.95$, the small tertiary structure (created by an evaporating droplet) was linked via a tendril to the primary structure [Fig. 9(h)]. At $c = 0.90$, the curved secondary structure forms a complete toroid which envelops the conical primary-tertiary structure, with the tertiary structure forming the point [Fig. 10(h)]. This point of the conical structure is predominantly comprised of points from the highest values of N_{cc}, while the portion of the toroid furthest from the secondary structure at $c = 0.96$ is all from cluster 16: the lowest values of N_{cc}. Therefore, the clusters have demonstrated the extent of this complex structure, which is principally responsible for global extinction commencing.

For $c \leq 0.80$, all the isosurfaces are approximately spherical (except for cases KG and F2, where they always remain oblong owing to the higher turbulence), so the evaporation is clearly weak that far from the spark centre. Droplets were initialised $0.25 \leq x \leq 0.75$, so there is the potential for droplets to be observed everywhere $c > 0.02$, since the isosurfaces for $c = 0.02$ do not reach the boundaries $0.4 \leq x \leq 0.6$ in the droplet cases. The clusters which are formed for $0.2 < c < 0.8$ generally span a relatively-large range of values of c, which accounts for the majority of the flame thickness (Figure 10 [35]), so there is a patchwork of clusters for each value of c. However, there is a tendency for clusters to persist in the radial direction as opposed to the transverse direction.

Clusters 10–15 for some of the cases are shown in Figs. 11–14; almost all the other clusters for the selected cases and the other cases are approximately spherical (besides the high-turbulence KG and F2 cases). The most important aspect that can be observed from these plots is clusters 10 and 12 from the Base case, Fig. 11(a) and (c), which are identified as being from the extinguishing branch, Fig. 7(d). These clusters combined are the equivalent structure seen in cases BE and I1 in Figs. 8–10 that wraps around the primary kernel and form the region of local extinction in the Base case. Statistically, this secondary structure cannot be distinguished from the primary kernel in cases BE and I1. This is because values of higher c were only present closer to the centre of the spark, while the secondary structure itself is smaller and closer to the centre than in the Base case. There is no inkling of this secondary structure in any of the visualisations of cases B1 and B2, which showed no local extinction.

Other notable features in the cluster visualisation are for case I1 in Fig. 13(f), where an isolated node corresponds to the location of a droplet [Fig. 8(g)], so the action of this evaporation links the behaviour of this location with the primary kernel. Case I2 has some unusual structures and the perspective is misleading in Fig. 14(b) and (c). Cluster 11 has two large, curved surfaces [which are seen to be separated in Fig. 14(b)], predominantly in the x-z plane; the bigger structure is at higher y (visualised on the left) and is further from the centre than the smaller structure. Cluster 12 consists of two rings roughly in the x-z plane (not the y-z plane as caused by the optical illusion of the perspective), connected by a curved surface at low z; the surfaces in cluster 11 fill the holes in cluster 12.

4. Conclusions

A data mining technique for analysing the fields produced by DNS has been utilised. The Gaussian Mixture Model groups data points which behave similarly. This technique has enabled confirmation of the bimodal behaviour at the highest values of c for a flame which shows local extinction-reignition behaviour. Specifically, the extinguishing and burning branches categorically demonstrate distinct behaviours. The extinguishing branch is identified to be due to evaporating droplets producing very rich mixtures in a curved region on one side of the spark centre, hence causing local quenching as indicated by the very low values of N_{cc}. However, this local quenching occurs on the edge of a very large flame kernel, which is able to provide a substantial flame front that has advanced approximately the same distance as the local quenching region. There is therefore sufficient energy to evaporate the droplets and heat the flammable mixture to produce a self-sustaining flame which reignites the locally-extinguished region.

In contrast, the flames which ignite but subsequently extinguish do not have evaporating droplets which cause local quenching. The droplets are outside a relatively-small flame kernel and are therefore necessary for flame propagation, rather than being supported by a substantial flame front which has advanced to a similar extent. Because the evaporative heat loss outweighs the chemical potential energy in the evaporated fuel, self-sustaining flame fronts are not produced: local extinction is followed by global extinction.

The results show that it is possible to identify local extinction (via different behaviours producing layers of clusters at intermediate values of c) and predict whether reignition will occur in the future (via bimodal behaviours producing layers of clusters at the highest values of c).

One of the limitations of the results is that single-step chemistry has been used, which is unable to capture all the physics of ignition. Future work will investigate the behaviour of these systems using multi-step chemistry. In addition, because these results are all from moderately-sparse droplet fields, future work will include assessing the behaviour for dense droplet fields.

Acknowledgment

The author is grateful to Prof. R. S. Cant for the usage of the SENGA code.

References

[1] R. Anderson, A New Direct Injection Spark Ignition (DISI) Combustion System for Low Emissions, Technical Report P0201, FISITA, 1996.

[2] R. B. R. da Costa, F. A. R. Filho, C. J. Coronado, A. F. Teixeira, N. A. D. Netto, Research on hydrous ethanol stratied lean burn combustion in a DI spark-ignition engine, Appl. Therm. Eng. 139 (2018) 317–324.

[3] S. Hemdal, Characterization of stratified fuel distribution and charge mixing in a DISI engine using Rayleigh scattering, Combust. Flame 193 (2018) 218–228.

[4] L. G. Clark, S. Kook, Q. N. Chan, E. R. Hawkes, The Effect of Fuel-Injection Timing on In-cylinder Flow and Combustion Performance in a Spark-Ignition Direct-Injection (SIDI) Engine Using Particle Image Velocimetry (PIV), Flow, Turbul. Combust. 101 (2018) 191–218.

[5] P. C. Ma, T. Ewan, C. Jainski, L. Lu, A. Dreizler, V. Sick, M. Ihme, Development and Analysis of Wall Models for Internal Combustion Engine Simulations Using High-speed Micro-PIV Measurements, Flow, Turbul. Combust. 28 (2017) 283–309.

[6] P. Aleiferis, M. Behringer, Modulation of integral length scales of turbulence in an optical SI engine by direct injection of gasoline, iso-octane, ethanol and butanol fuels, Fuel 189 (2017) 238–259.

[7] A. Kourmatzis, P. X. Pham, A. R. Masri, Characterization of atomization and combustion in moderately dense turbulent spray flames, Combust. Flame 162 (2015) 978–996.

[8] C. T. Chong, S. Hochgreb, Spray and combustion characteristics of biodiesel: Non-reacting and reacting, Int. Biodeter. Biodegr. 102 (2015) 353–360.

[9] Y. Pei, E. R. Hawkes, M. Bolla, S. Kook, G. M. Goldin, Y. Yang, S. B. Pope, S. Som, An analysis of the structure of an n-dodecane spray flame using TPDF modelling, Combust. Flame 168 (2016) 420–435.

[10] H. A. El-Asrag, M. Braun, A. R. Masri, Large eddy simulations of partially premixed ethanol dilute spray flames using the flamelet generated manifold model, Combust. Theor. Model. 20 (2016) 567–591.

[11] T. Marchione, S. Ahmed, E. Mastorakos, Ignition of Turbulent Swirling *n*-heptane Spray Flames using Single and Multiple Sparks, Combust. Flame 156 (2009) 166–180.

[12] W. P. Jones, A. Tyliszczak, Large Eddy Simulation of Spark Ignition in a Gas Turbine Combustor, Flow, Turbul. Combust. 85 (2010) 711–734.

[13] R. W. Bilger, A Mixture Fraction Framework for the Theory and Modeling of Droplets and Sprays, Combust. Flame 158 (2011) 191–202.

[14] E. Mastorakos, Ignition of Turbulent Non-premixed Flames, Progr. Energy Combust. Sci. 35 (2009) 57–97.

[15] P. Jenny, D. Roekaerts, N. Beishuizen, Modeling of Turbulent Dilute Spray Combustion, Progr. Energy Combust. Sci. 38 (2012) 846–887.

[16] A. Giusti, M. Sitte, G. Borghesi, E. Mastorakos, Numerical investigation of kerosene single droplet ignition at high-altitude relight conditions, Fuel 225 (2018) 663–670.

[17] J. Réveillon, L. Vervisch, Analysis of Weakly Turbulent Dilute-Spray Flames and Spray Combustion Regimes, J. Fluid Mech. 537 (2005) 317–347.

[18] L. C. Selle, J. Bellan, Evaluation of Assumed-PDF Methods in Two-phase Flows using Direct Numerical Simulation, Proc. Combust. Inst. 31 (2007) 2273–2281.

[19] Y. Wang, C. J. Rutland, Direct numerical simulation of ignition in turbulent *n*-heptane liquid fuel spray jets, Combust. Flame 149 (2007) 353–365.

[20] P. Schroll, A. P. Wandel, R. S. Cant, E. Mastorakos, Direct Numerical Simulations of Autoignition in Turbulent Two-phase Flows, Proc. Combust. Inst. 32 (2009) 2275–2282.

[21] A. Neophytou, E. Mastorakos, R. S. Cant, Complex Chemistry Simulations of Spark Ignition in Turbulent Sprays, Proc. Combust. Inst. 33 (2011) 2135–2142.

[22] E. Demosthenous, G. Borghesi, E. Mastorakos, R. S. Cant, Direct Numerical Simulations of premixed methane flame initiation by pilot n-heptane spray autoignition, Combust. Flame 163 (2016) 122–137.

[23] D. H. Wacks, N. Chakraborty, E. Mastorakos, Statistical Analysis of Turbulent Flame-Droplet Interaction: A Direct Numerical Simulation Study, Flow, Turbul. Combust. 96 (2016) 573–607.

[24] D. H. Wacks, N. Chakraborty, Flame Structure and Propagation in Turbulent Flame-Droplet Interaction: A Direct Numerical Simulation Analysis, Flow, Turbul. Combust. 96 (2016) 1053–1081.

[25] A. Abdelsamie, D. Thévenin, Direct numerical simulation of spray evaporation and autoignition in a temporally-evolving jet, Proc. Combust. Inst. 36 (2017) 2493–2502.

[26] B. Duret, G. Luret, J. Reveillon, T. Menard, A. Berlemont, F. X. Demoulin, DNS analysis of turbulent mixing in two-phase flows, Int. J. Multiphase Flow 40 (2012) 93–105.

[27] B. Duret, J. Reveillon, T. Menard, F. X. Demoulin, Improving primary atomization modeling through DNS of two-phase flows, Int. J. Multiphase Flow 55 (2013) 130–137.

[28] Z. Bouali, B. Duret, F.-X. Demoulin, A. Mura, DNS Analysis of Small-scale Turbulence-Scalar Interactions in Evaporating Two-Phase Flows, Int. J. Multiphase Flow 85 (2016) 326–335.

[29] M. R. Zoby, S. Navarro-Martinez, A. Kronenburg, A. Marquis, Evaporation Rates of Droplet Arrays in Turbulent Reacting Flows, Proc. Combust. Inst. 33 (2011) 2117–2125.

[30] M. R. Zoby, S. Navarro-Martinez, A. Kronenburg, A. Marquis, Turbulent Mixing in Three-dimensional Droplet Arrays, Int. J. Heat Fluid Flow 32 (2011) 499–509.

[31] J. Shinjo, A. Umemura, Droplet/Turbulence Interaction and Early Flame Kernel Development in an Autoigniting Realistic Dense Spray, Proc. Combust. Inst. 34 (2013) 1553–1560.

[32] J. Shinjo, J. Xia, L. C. Ganippa, A. Megaritis, Puffing-enhanced fuel/air mixing of an evaporating n-decane/ethanol emulsion droplet and a droplet group under convective heating, J. Fluid Mech. 793 (2016) 444–476.

[33] B. Wang, A. Kronenburg, D. Dietzel, O. T. Stein, Assessment of scaling laws for mixing fields in inter-droplet space, Proc. Combust. Inst. 36 (2017) 2451–2458.

[34] A. P. Wandel, Extinction Predictors in Turbulent Sprays, Proc. Combust. Inst. 34 (2013) 1625–1632.

[35] A. P. Wandel, Influence of Scalar Dissipation on Flame Success in Turbulent Sprays with Spark Ignition, Combust. Flame 161 (2014) 2579–2600.

[36] K. W. Jenkins, R. S. Cant, DNS of Turbulent Flame Kernels, in: Proceedings of the Second AFOSR Conference on DNS and LES, Kluwer Academic, 1999, pp. 192–202.

[37] N. Chakraborty, E. Mastorakos, Numerical Investigation of Edge Flame Propagation Characteristics in Turbulent Mixing Layers, Phys. Fluids 18 (2006) 105103.

[38] N. Chakraborty, E. Mastorakos, R. S. Cant, Effects of Turbulence on Spark Ignition in Inhomogeneous Mixtures: A Direct Numerical Simulation (DNS) Study, Combust. Sci. Tech. 179 (2007) 293–317.

[39] N. Chakraborty, E. Mastorakos, Direct Numerical Simulations of Localised Forced Ignition in Turbulent Mixing Layers: The Effects of Mixture Fraction and Its Gradient, Flow, Turbul. Combust. 80 (2008) 155–186.

[40] A. P. Wandel, N. Chakraborty, E. Mastorakos, Direct Numerical Simulations of Turbulent Flame Expansion in Fine Sprays, Proc. Combust. Inst. 32 (2009) 2283–2290.

[41] T. J. Poinsot, S. K. Lele, Boundary Conditions for Direct Simulation of Compressible Viscous Flows, J. Comput. Phys. 101 (1992) 104–129.

[42] A. A. Wray, Minimal storage time advancement schemes for spectral methods, 1992. Unpublished Report.

[43] R. S. Rogallo, Numerical Experiments in Homogeneous Turbulence, Technical Report NASA Technical Memorandum 81315, NASA Ames Research Center, 1981.

[44] G. K. Batchelor, A. A. Townsend, Decay of Turbulence in Final Period, Proc. Royal Soc. London A 194 (1948) 527–543.

[45] R. W. Bilger, The Structure of Turbulent Nonpremixed Flames, Proc. Combust. Inst. 23 (1988) 475.

[46] M. Kantardzic, Data Mining: Concepts, Models, Methods and Algorithms, IEEE Press, second edition, 2011.

[47] D. Reynolds, in: Encyclopedia of Biometrics, Springer, 2009, pp. 659–663.

[48] A. Neophytou, E. Mastorakos, R. S. Cant, The Internal Structure of Igniting Turbulent Sprays as Revealed by Complex Chemistry DNS, Combust. Flame 159 (2012) 641–664.

[49] H. H. Chiu, T. M. Liu, Group Combustion of Liquid Droplets, Combust. Sci. Tech. 17 (1977) 127–142.

[50] J. Han, M. Kamber, J. Pei, Data Mining: Concepts and Techniques, Elsevier, third edition, 2012.

[51] S. K. Aggarwal, A review of spray ignition phenomena: present status and future research, Progr. Energy Combust. Sci. 24 (1998) 565–600.

Figures

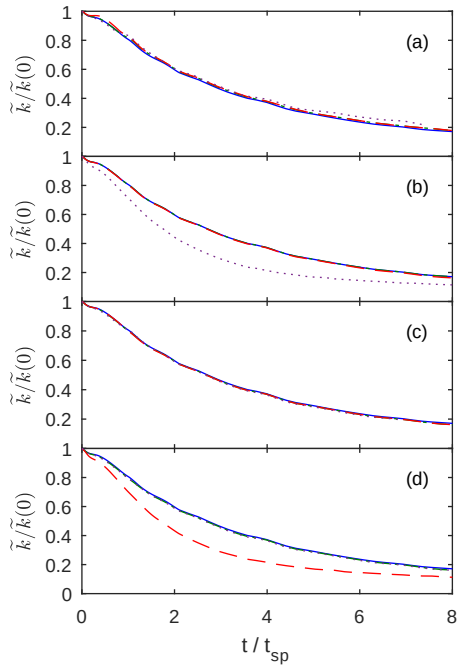

Figure 1: Favre-mean turbulent kinetic energy, normalised by initial turbulent kinetic energy. Base case is shown in all plots: —. Other cases: (a) B1, – ·; B2, – –; BG, · · · . (b) BE, – –; KG, · · · . (c) I1, – ·; I2, – –; IG, · · · . (d) F1, – ·; F2, – –; FG, · · · .

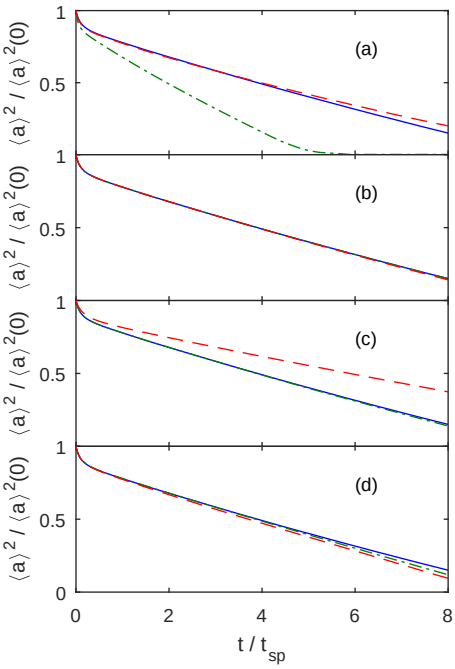

Figure 2: Square of mean droplet diameter for droplets still in the domain, normalised by initial droplet diameter. Base case is shown in all plots: —. Other cases: (a) B1, – ·; B2, – –. (b) BE, – –. (c) I1, – ·; I2, – –. (d) F1, – ·; F2, – –.

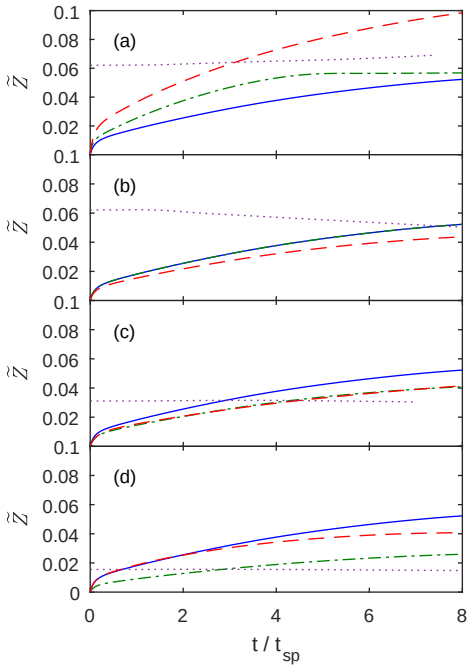

Figure 3: Favre-mean mixture fraction for the whole domain. Base case is shown in all plots: —. Other cases: (a) B1, – ·; B2, – –; BG, · · · ·. (b) BE, – –; KG, · · · ·. (c) I1, – ·; I2, – –; IG, · · · ·. (d) F1, – ·; F2, – –; FG, · · · ·.

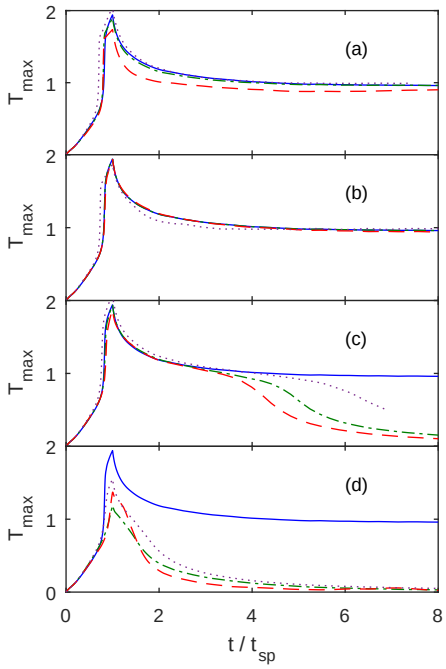

Figure 4: Maximal temperature in the whole domain. Base case is shown in all plots: —. Other cases: (a) B1, – ·; B2, – –; BG, · · · ·. (b) BE, – –; KG, · · · ·. (c) I1, – ·; I2, – –; IG, · · · ·. (d) F1, – ·; F2, – –; FG, · · · ·.

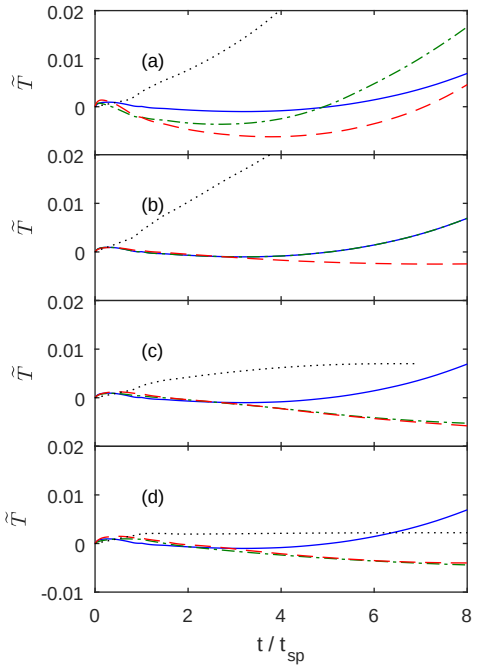

Figure 5: Favre-mean temperature for the whole domain. Base case is shown in all plots: —. Other cases: (a) B1, – ·; B2, – –; BG, · · · . (b) BE, – –; KG, · · · . (c) I1, – ·; I2, – –; IG, · · · . (d) F1, – ·; F2, – –; FG, · · · .

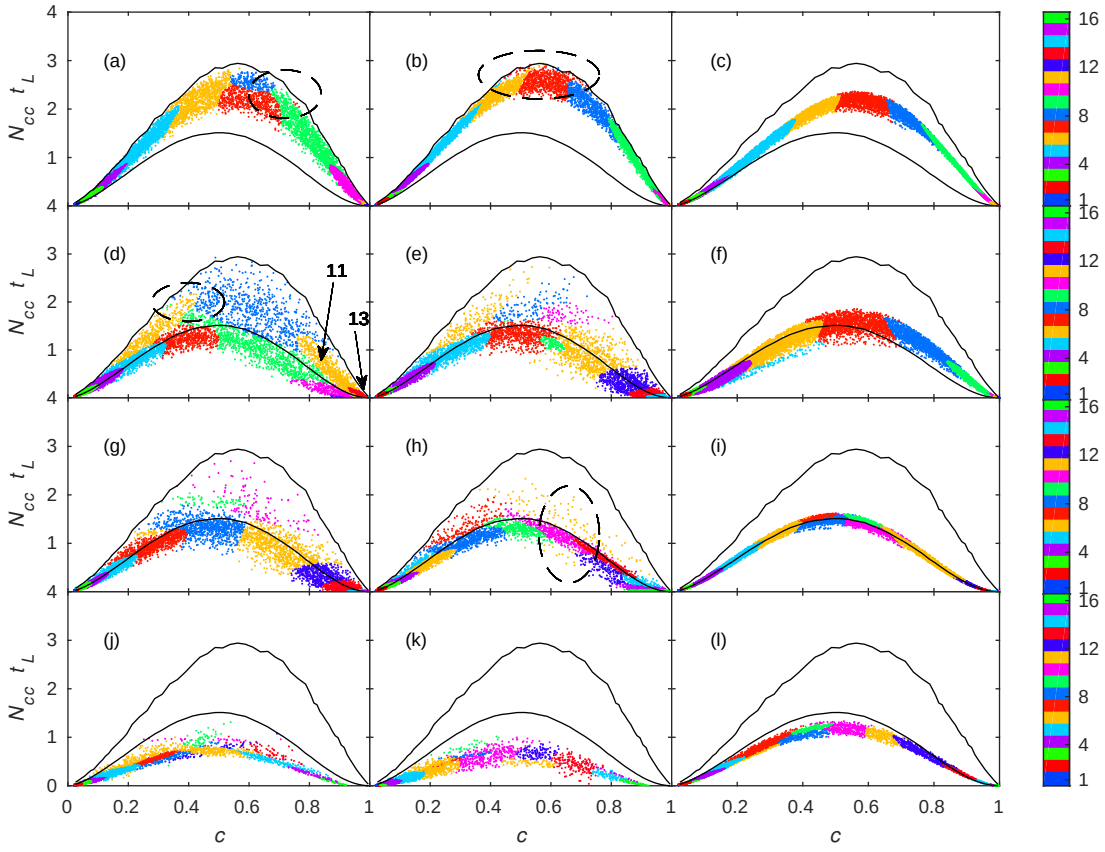

Figure 6: Cluster plots when the spark was deactivated. The first two columns are droplet cases, while the third column contains gaseous cases; rows contain cases as grouped in Table 2. The colour for each cluster is shown on the right. Clusters are numbered based on increasing values of $\boldsymbol{\mu}_i$ for variable c. The upper black line is the conditional maximum for case B2; the lower black line is the conditional mean for case IG. The dashed ellipses show regions where data within a cluster is separated from other data within the same cluster; some clusters are identified in (b). Cases (and cluster containing the largest N_{cc}): (a) B1 (6); (b) B2 (7); (c) BG (7); (d) Base (8); (e) BE (6); (f) KG (7); (g) I1 (10); (h) I2 (11); (i) IG (7); (j) F1 (9); (k) F2 (10); (l) FG (10).

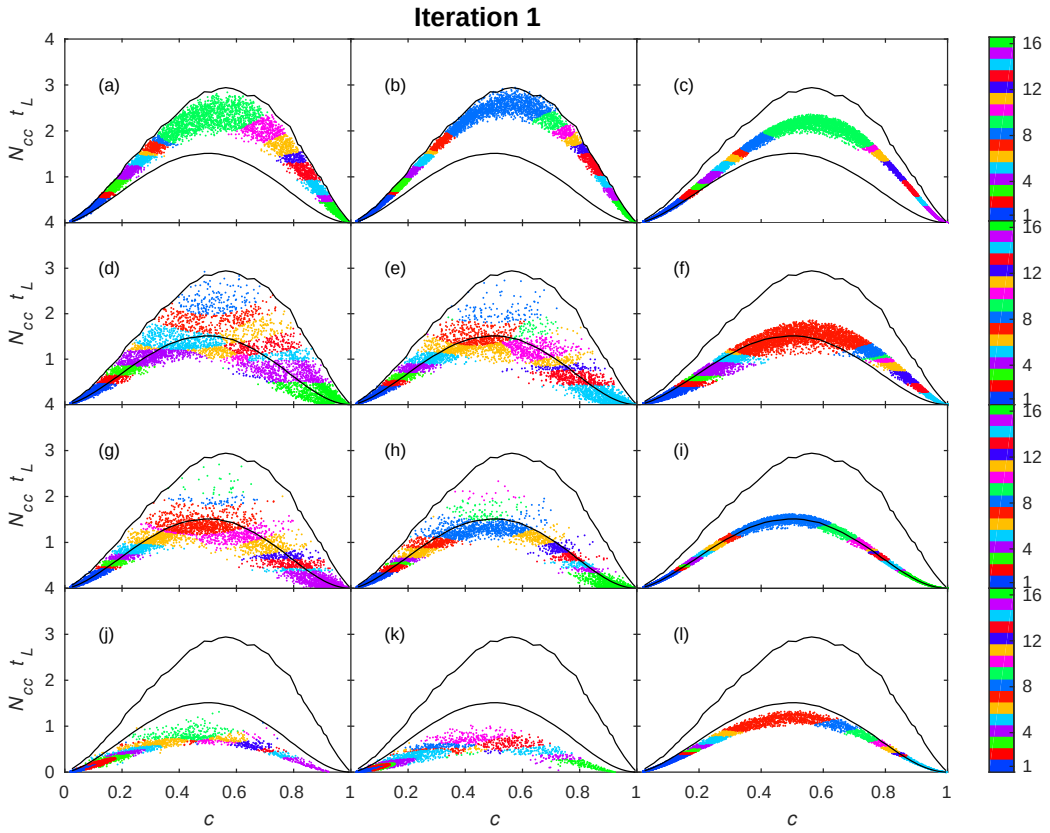

Video 1: Video of convergence history of cluster plots for $M = 16$. The animation progressively accelerates through the iterations and freezes for each case once convergence is reached for that case. The first two columns are droplet cases, while the third column contains gaseous cases; rows contain cases as grouped in Table 2. The colour for each cluster is shown on the right. Clusters are numbered based on increasing values of $\boldsymbol{\mu}_i$ for variable c. The upper black line is the conditional maximum for case B2; the lower black line is the conditional mean for case IG. Cases: (a) B1; (b) B2; (c) BG; (d) Base; (e) BE; (f) KG; (g) I1; (h) I2; (i) IG; (j) F1; (k) F2; (l) FG.

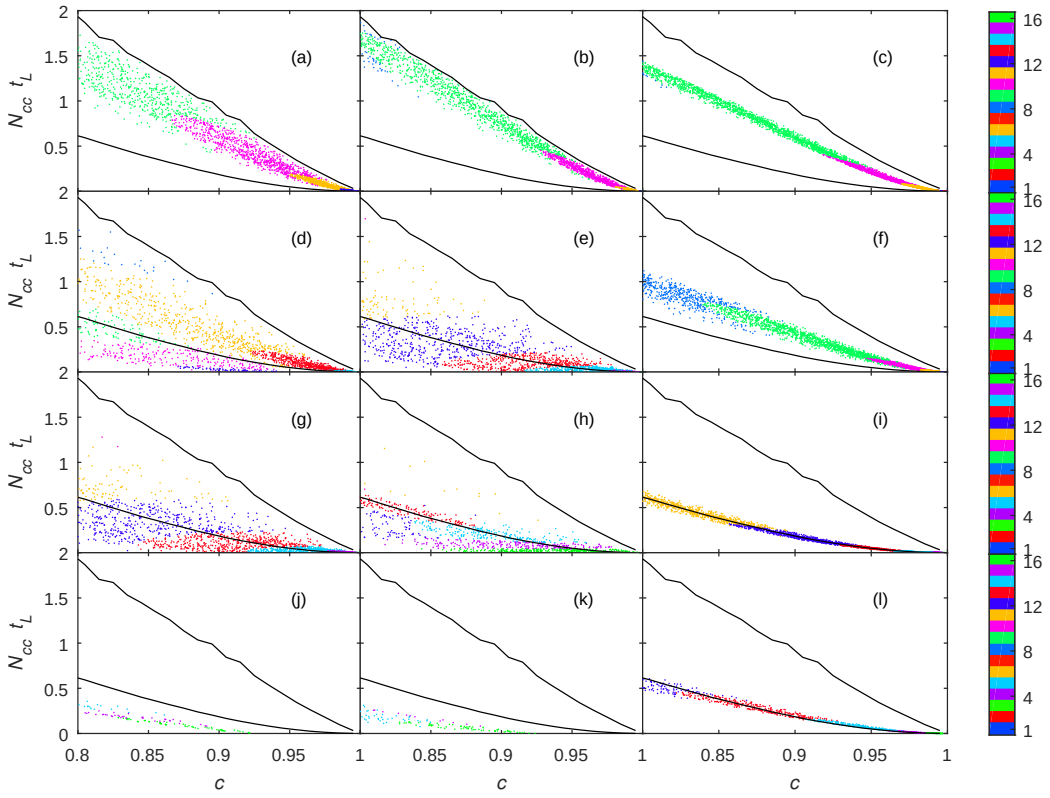

Figure 7: Replication of Fig. 6, zoomed in on the bottom-right corner. Cases (and lowest cluster shown): (a) B1 (9); (b) B2 (8); (c) BG (8); (d) Base (8); (e) BE (10); (f) KG (8); (g) I1 (10); (h) I2 (11); (i) IG (11); (j) F1 (14); (k) F2 (14); (l) FG (12).

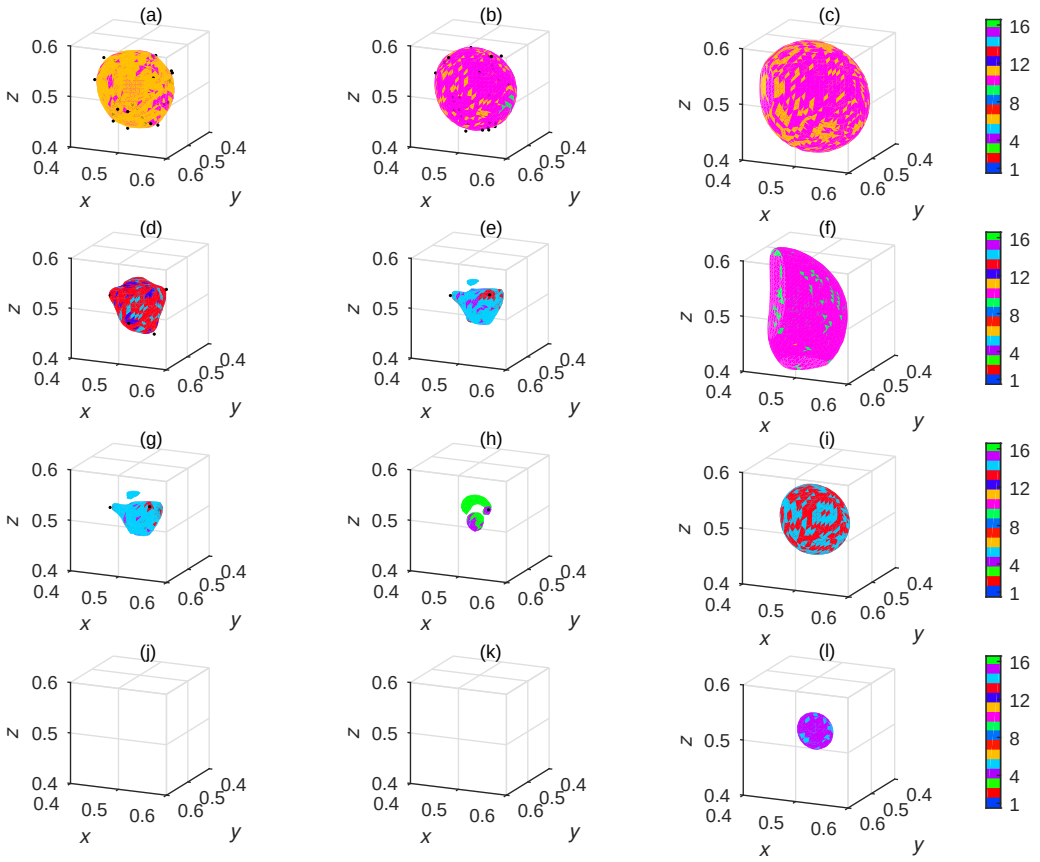

Figure 8: Isosurface of $c = 0.96$ when the spark was deactivated, coloured by cluster. Black dots represent droplets which are close to the isosurface. Cases (and clusters shown): (a) B1 (10–11); (b) B2 (9–11); (c) BG (10–11); (d) Base (12–14); (e) BE (13–15); (f) KG (9–10); (g) I1 (13–15); (h) I2 (15–16); (i) IG (13–14); (j) F1 (no locations with $c = 0.96$); (k) F2 (no locations with $c = 0.96$); (l) FG (14–15).

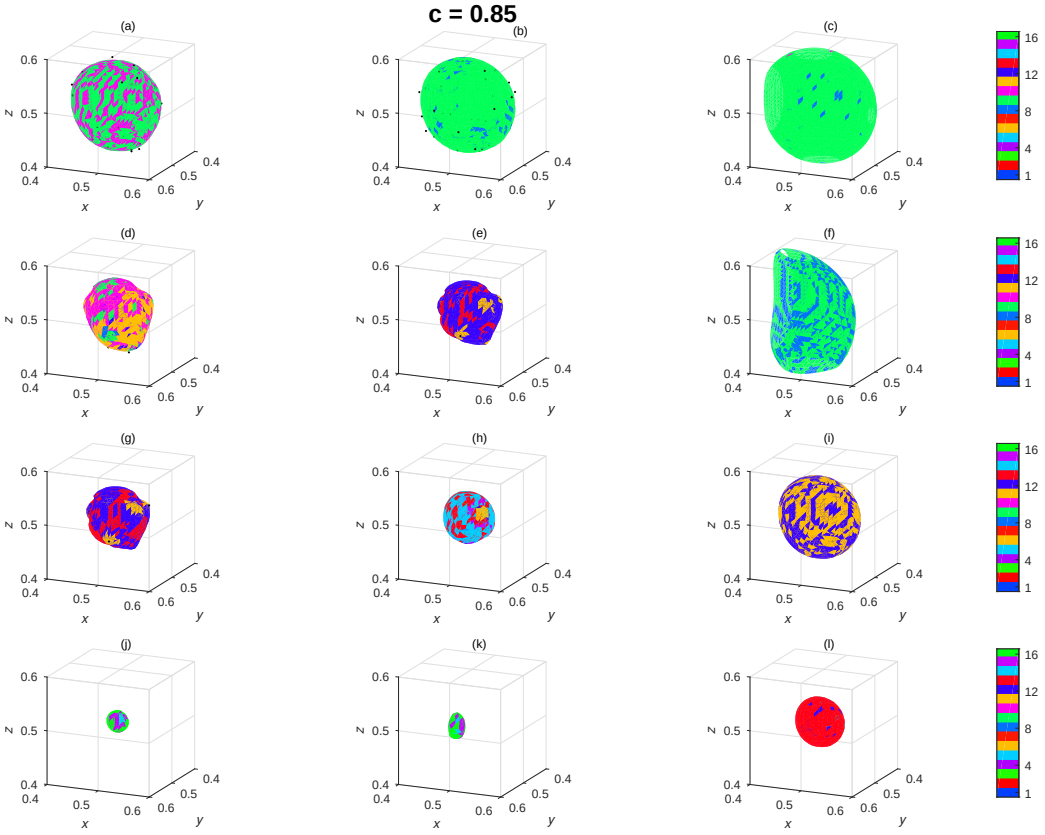

Video 2: Video of isosurfaces of c when the spark was deactivated, coloured by cluster. Black dots represent droplets which are close to the isosurface. Cases: (a) B1; (b) B2; (c) BG; (d) Base; (e) BE; (f) KG; (g) I1; (h) I2; (i) IG; (j) F1; (k) F2; (l) FG. Holes observed in (c) and (f) for low c are due to the isosurfaces extending beyond the small box visualised.

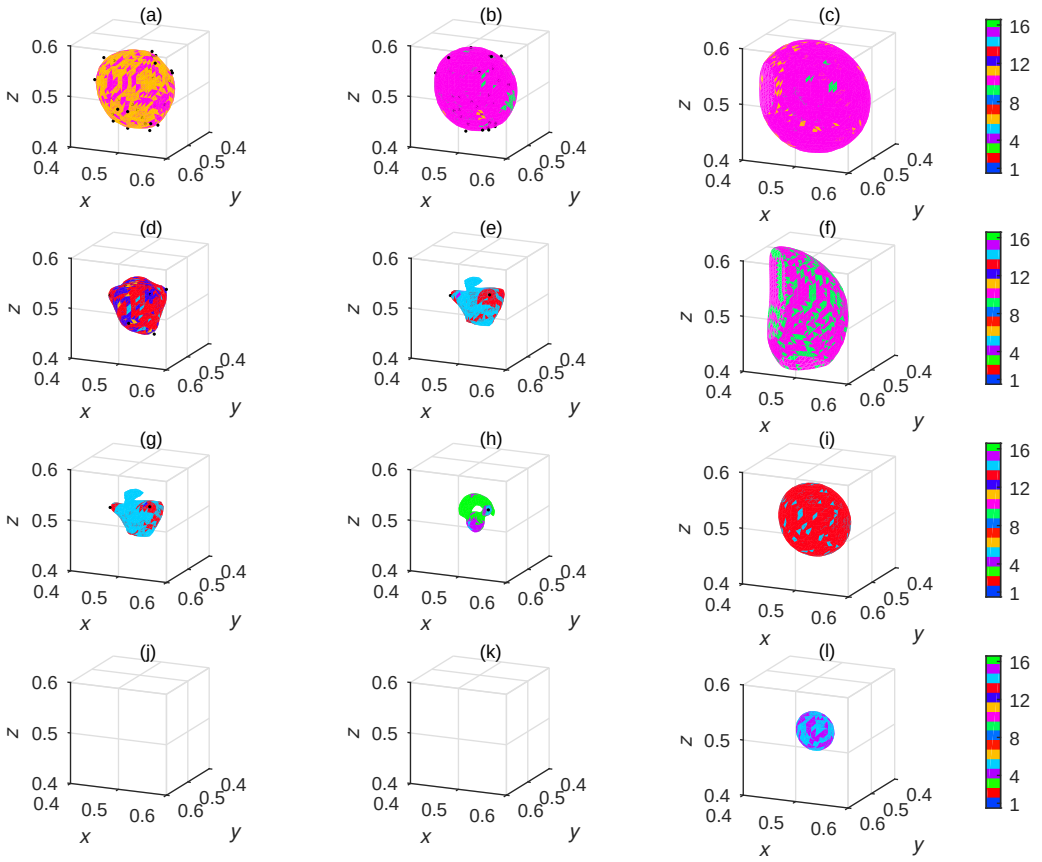

Figure 9: Isosurface of $c = 0.95$ when the spark was deactivated, coloured by cluster. Black dots represent droplets which are close to the isosurface. Cases (and clusters shown): (a) B1 (10–11); (b) B2 (9–11); (c) BG (9–11); (d) Base (11–14); (e) BE (13–15); (f) KG (9–10); (g) I1 (12–14); (h) I2 (14–16); (i) IG (13–14); (j) F1 (no locations with $c = 0.95$); (k) F2 (no locations with $c = 0.95$); (l) FG (14–15).

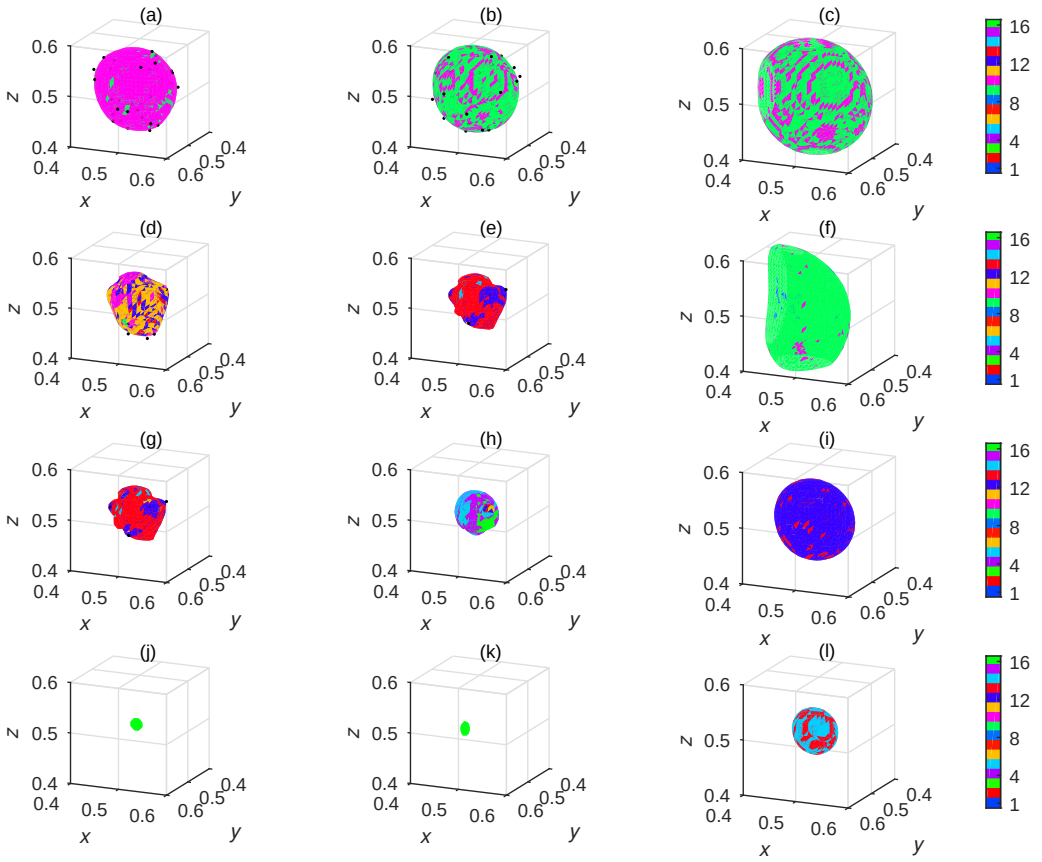

Figure 10: Isosurface of $c = 0.90$ when the spark was deactivated, coloured by cluster. Black dots represent droplets which are close to the isosurface. Cases (and clusters shown): (a) B1 (9–10); (b) B2 (9–10); (c) BG (9–10); (d) Base (9–13); (e) BE (12–14); (f) KG (8–10); (g) I1 (11–14); (h) I2 (11–15); (i) IG (12–13); (j) F1 (16); (k) F2 (16); (l) FG (13–14).

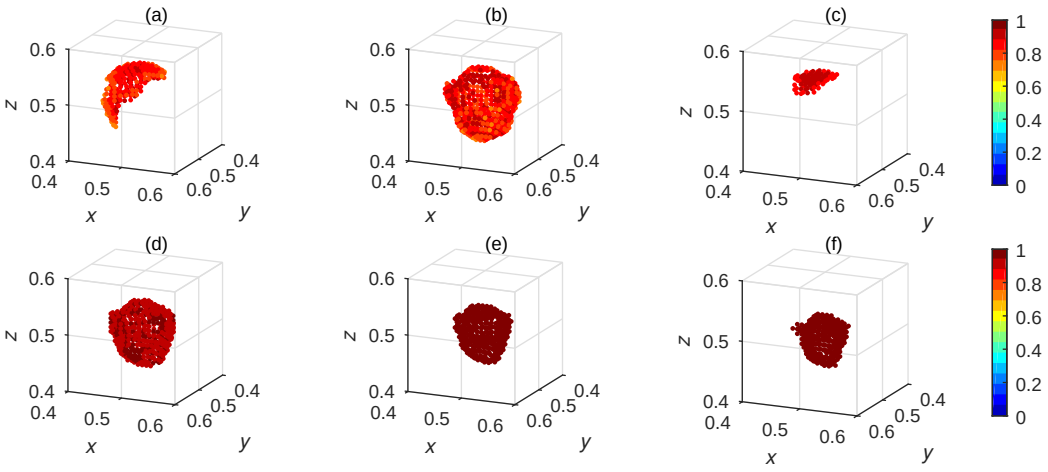

Figure 11: Selected clusters for Base case, coloured by c. Clusters: (a) 10; (b) 11; (c) 12; (d) 13; (e) 14; (f) 15.

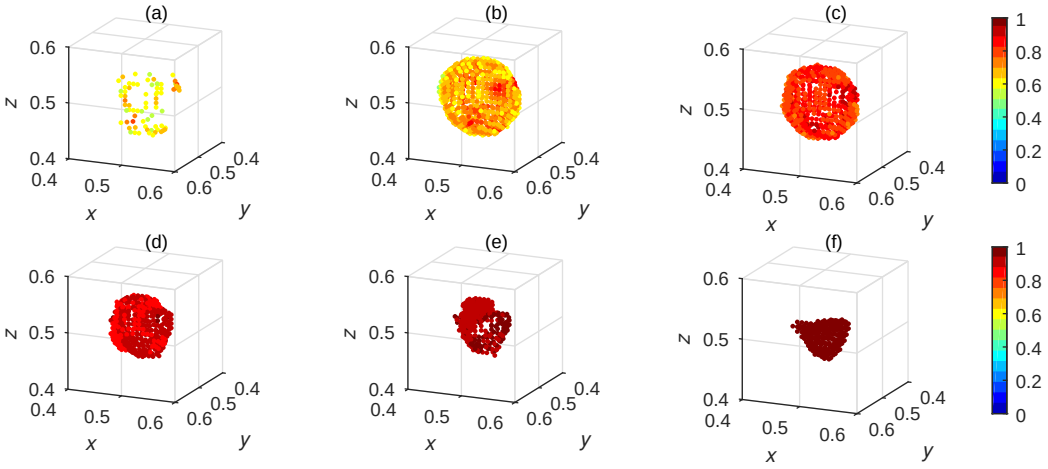

Figure 12: Selected clusters for case BE, coloured by c. Clusters: (a) 10; (b) 11; (c) 12; (d) 13; (e) 14; (f) 15.

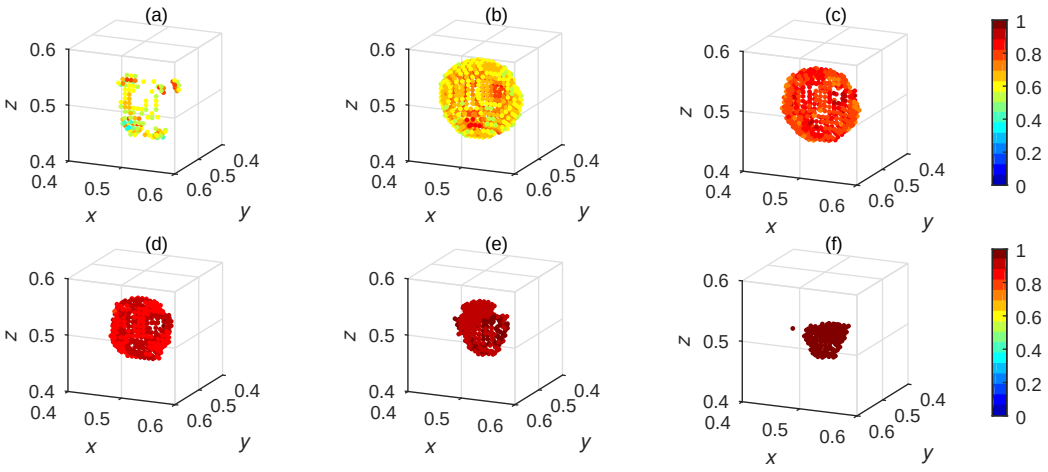

Figure 13: Selected clusters for case I1, coloured by c. Clusters: (a) 10; (b) 11; (c) 12; (d) 13; (e) 14; (f) 15.

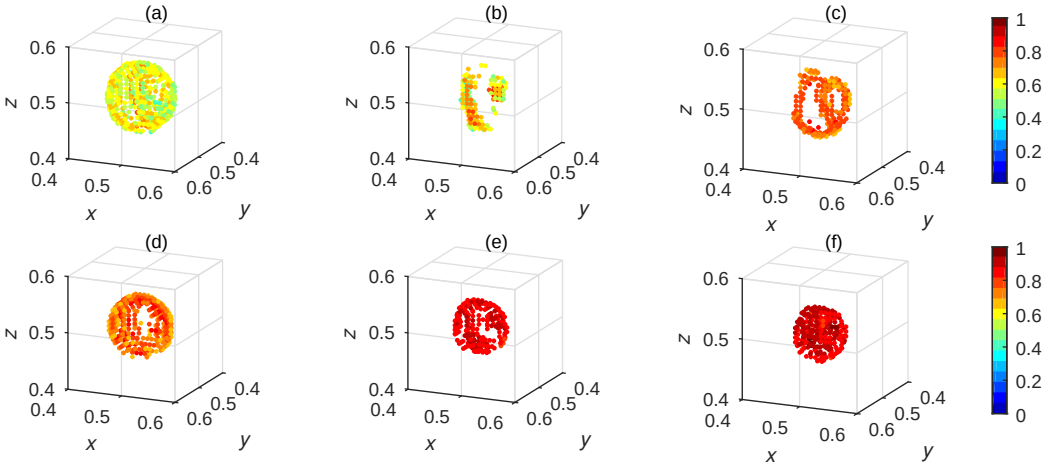

Figure 14: Selected clusters for case I2, coloured by c. Clusters: (a) 10; (b) 11; (c) 12; (d) 13; (e) 14; (f) 15.